



HAL
open science

Optimized multimodal nanoplatfoms for targeting $\alpha v\beta 3$ integrins

Julie Bolley, Yoann Lalatonne, Oualid Haddad, Didier Letourneur, Michael Soussan, Joelle Pérard-Viret, Laurence Motte

► **To cite this version:**

Julie Bolley, Yoann Lalatonne, Oualid Haddad, Didier Letourneur, Michael Soussan, et al.. Optimized multimodal nanoplatfoms for targeting $\alpha v\beta 3$ integrins. *Nanoscale*, 2013, 5 (23), pp.11478. 10.1039/C3NR03763K . hal-03385035

HAL Id: hal-03385035

<https://hal.science/hal-03385035>

Submitted on 19 Oct 2021

HAL is a multi-disciplinary open access archive for the deposit and dissemination of scientific research documents, whether they are published or not. The documents may come from teaching and research institutions in France or abroad, or from public or private research centers.

L'archive ouverte pluridisciplinaire **HAL**, est destinée au dépôt et à la diffusion de documents scientifiques de niveau recherche, publiés ou non, émanant des établissements d'enseignement et de recherche français ou étrangers, des laboratoires publics ou privés.

Optimized multimodal nanoplatforms for targeting $\alpha_v\beta_3$ integrins†

Julie Bolley,^a Yoann Lalatonne,^{ab} Oualid Haddad,^c Didier Letourneur,^c Michael Soussan,^b Joelle Pérard-Viret^d and Laurence Motte^{*a}

Magnetic Resonance Imaging (MRI) using contrast agents is a very powerful technique for diagnosis in clinical medicine and biomedical research. The synthesis of ultrasmall superparamagnetic iron oxide (USPIO) nanoparticles targeting $\alpha_v\beta_3$ integrins and acting as new MRI contrast agents seems to be a promising way for cancer diagnosis. Indeed, it is well established that $\alpha_v\beta_3$ integrin plays a key role in tumor angiogenesis acting like a receptor for the extracellular matrix proteins like vitronectin, fibronectin through the arginine-glycine-aspartic acid (RGD) sequence. Up-regulation of $\alpha_v\beta_3$ has been found to be associated with a wide range of cancers, making it a broad-spectrum tumor-marker. In this study, USPIO nanocrystals were synthesized and surface passivated with caffeic acid. The large number of the carboxylic acid functions at the outer surface of the nanoplatforms was used for the covalent coupling of Rhodamine123, polyethylene glycol (PEG) and cyclic RGD. Soluble carbodiimide (EDC) and *N*-hydroxysuccinimide (NHS) were used to crosslink carboxylic acid with the amino group of the ligands. We examined the design of the nanoplatforms with each individual entity and then the combination of two and three of them. Several methods were used to characterize the nanoparticle surface functionalization and the magnetic properties of these contrast agents were studied using a 1.5 T clinical MRI scanner. The affinity towards integrins was evidenced by surface plasmon resonance and solid-phase receptor-binding assay.

Introduction

Targeted superparamagnetic iron oxide nanoparticles¹ (SPIONs) are an exciting class of materials that are undergoing clinical development as diagnostic,^{2,3} molecular imaging probes⁴ and therapeutic delivery vehicles.⁵ The use of these nanomaterials in biomedicine requires the ability to finely tune the surface functionality to provide the selective or specific recognition required for bio sensing.

Active targeting methods generally involve covalently attaching a targeting ligand to the surface of a biocompatible

coating.^{6,7} This facilitates for instance the active targeting of a cancer cell biomarker and allows SPIONs to accumulate in the cancer cells. The result is a better contrast between the tumor and healthy tissues on a MR image. In addition, multivalent interactions between the nanoparticles and their targets can increase the affinity of target binding (avidity).⁸

Integrin $\alpha_v\beta_3$ are cell adhesion molecules known to be involved in multiple steps of cancer angiogenesis, in cancer cell proliferation and metastatic diffusion, in angiogenesis in ischemic tissues, in atherosclerotic damage and in vascular restenosis, as well as in osteoporosis.^{9,10} The high expression of integrin $\alpha_v\beta_3$ during tumor growth, invasion and metastasis makes it an interesting molecular target for the development of $\alpha_v\beta_3$ targeted therapeutic drugs and molecular imaging probes. It is also highly expressed by several solid tumors such as glioblastomas, melanomas, and ovarian, breast, and prostate cancers, where it is involved in processes governing metastasis.^{11,12} Monoclonal antibodies, cyclic RGD (Arg-Gly-Asp) peptides and peptidomimetic antagonists have been shown for their potential as therapeutic pharmaceuticals, inhibiting endothelium-specific integrin survival signaling.^{13,14} RGD has been recognized as the minimal integrin sequence for the preferential binding to $\alpha_v\beta_3$ integrin. The cyclization is commonly employed to improve the binding properties of RGD peptides, conferring rigidity to the structure and preventing

^aUniversité Paris 13, Sorbonne Paris Cité, Laboratoire CSPBAT, CNRS (UMR 7244), 74 avenue M. Cachin, 93017 Bobigny, France. E-mail: Laurence.motte@univ-paris13.fr; Fax: +33 1 41 08 85 28

^bDepartment of Nuclear Medicine, Avicenne Hospital, Université Paris 13, Sorbonne Paris Cité, 74 avenue M. Cachin, 93017 Bobigny, France

^cINSERM, U698, 46 rue Henri Huchard, 75877 Paris Cedex 18, France

^dUniversité Paris Descartes, Sorbonne Paris Cité, Faculté de Pharmacie, CNRS (UMR 8638), 4 avenue de l'observatoire, 75240 Paris cedex 06, France

† Electronic supplementary information (ESI) available: TEM image and size distribution of $\gamma\text{Fe}_2\text{O}_3$ @CA nanoplatforms, determination of CA number per nanoparticle, dye R123, NH_2 -PEG-COOH and cRGD derivative coupling, biological stability, SPR analysis – theoretical analyte binding capacity, solid phase binding assay – determination of echistatin K_d . See DOI: 10.1039/c3nr03763k

chemical degradation. cRGDfK and cRGDyK with lysine and tyrosine residues respectively can be used for further chemical conjugation reactions.⁹ It has also been shown that the binding of multivalent cyclic RGD peptides using dendrimers,¹⁵⁻¹⁷ polymers,¹⁸ liposomes,¹⁹ and nanoparticles²⁰ as substrates enhances the integrin $\alpha_v\beta_3$ affinity, inducing better targeting capability and higher cellular uptake through the integrin dependant endocytosis. Thus, by increasing the peptide multiplicity, they significantly enhance the avidity of the multiple ligands for the $\alpha_v\beta_3$ integrin with a trend that is frequently proportional to the number of RGD moieties.^{20,21}

One important challenge for nanomedicine is the development of targeted multimodal medical imaging that could be used for MRI, for quantification of the integrin $\alpha_v\beta_3$ expression level before and during the anti-angiogenic therapy or in the case of surgical removal of the tumour, capable of achieving high specificity and sensitivity by *in vivo* IR fluorescent imaging for guided surgery. To achieve these goals, particle surface engineering remains a key step for the bioactive nanoparticle design.

In this article, the development of functionalized iron oxide nanoparticles that orchestrate the dual imaging with magnetic resonance, fluorescence imaging and $\alpha_v\beta_3$ targeting through multivalent cRGDfK or cRGDfK-PEG₂-NH₂ linked to iron oxide nanoparticles, is reported. We focused on several characterization methods in order to qualitatively or quantitatively characterize the nanoparticle surface functionalization. The effect of the multivalency for the interactions between the cRGD ligand and the target $\alpha_v\beta_3$ receptor is studied by means of a Surface Plasmon Resonance (SPR) and a solid-phase receptor-binding assay. The influence of PEG linker and the contribution of the number of grafted cRGD per nanoparticle are discussed.

For this purpose, iron oxide nanoparticles (NPs) were surface functionalized with caffeic acid (CA), a catechol derivative. Caffeic acid is one of the principal sources of biomass.²² This nanoplatform was first designed with each individual entity: fluorescent Rhodamine, PEG chain and cyclic cRGD with or without PEG chain. In a second step the combination of various functionalities onto the nanoparticle surface was performed.

To our knowledge, multimodal nanoplatforms elaborated with caffeic acid have never been reported.

Rhodamine was used as the fluorescent moiety for conjugation considering low cost and remarkable stability of the optical properties under pH modification compared to commercially near infrared imaging agents.

Experimental section

Chemical and apparatus

The dye Rhodamine123 (R123), cRGD derivatives, cyclo(Arg-Gly-Asp-d-Phe-Lys) (cRGDfK) and cyclo(Arg-Gly-Asp-d-Phe-Lys(PEG-PEG)) (cRGDfK-(PEG)₂-NH₂), and integrin $\alpha_v\beta_3$ were purchased from Acros, Peptides International and Merck respectively. Carboxyl-(tetraethyleneglycol)ethylamine (H₂N-(PEG)₄-COOH) and fluoralddehyde OPA reagent solution were purchased from Thermoscientific. Fluoralddehyde OPA reagent solution contains 0.8 mg mL⁻¹ of *o*-phthalaldehyde (OPA), pH 10. Other

commercially available reagents for particles' synthesis and analyses were purchased from Sigma-Aldrich. For affinity measurements, the sensor chip CM5 was purchased from GE Healthcare.

The chemical coupling under microwaves was performed using a Monowave 300 (Anton Paar).

The infrared (IR) spectra of the caffeic acid (CA) and of the nanoplatforms $\gamma\text{Fe}_2\text{O}_3@CA$, $\gamma\text{Fe}_2\text{O}_3@CA\text{-R123}$, and $\gamma\text{Fe}_2\text{O}_3@CA\text{-PEG-COOH}$ were recorded as thin films on KBr pellets on a thermo scientific Nicolet 380 FTIR and are reported in frequency of absorption (cm⁻¹). The infrared spectra of cRGDfK before and after microwaves were recorded as a liquid sample using a Tensor 27 spectrophotometer (Bruker, Karlsruhe, Germany) at a 1 cm⁻¹ resolution.

UV-visible spectra were recorded on a Varian Cary 50 Scan UV-Visible spectrophotometer. The size and the zeta potential of the nanocomplex were determined by dynamic laser light scattering (DLS) on a Nano-ZS (Red Badge) ZEN 3600 device (Malvern Instruments, Malvern, UK).

TEM images were obtained using a FEI CM10 Microscope (Philips) and samples were prepared by depositing a drop of nanoparticle suspension on carbon coated copper grids placed on a filter paper. The median diameter was deduced from TEM data measurements, simulating the diameter distribution with a lognormal function.

The magnetic behavior of the as-synthesized nanoparticles was characterized at room temperature using a vibrating sample magnetometer, VSM (Quantum Design, Versalab) and a MIAplex® reader (Magnisense SA). The VSM measures the magnetization by cycling the applied field from -2300 to +2300 kA m⁻¹ for two times with a step rate of 8 kA s⁻¹. Measurements were performed on powder samples and the temperature was set to 298 K (25 °C) to study the behavior of the particles at room temperature. The MIAplex reader is a miniaturized chip detector system, measuring a signal corresponding to the second derivative of the magnetization around zero field.²³ With this sensor, measurements are performed on microliter sample volumes, in a handled portable device, without liquid helium cooling to operate. Moreover, MIAplex® signal measurement (~30 s) is about 10² times shorter than the VSM (~1 h) and the sample quantity is 10³ times lower (1 µg).

The MRI analyses were performed using a 1.5 T MRI scanner (Philips intera 1.5T/Philips healthcare) at room temperature for various iron concentrations. The longitudinal nuclear relaxation times *T*₁ were obtained from an inversion recovery sequence with a time repetition (TR) of 2000 ms, a time echo (TE) of 16 ms and increasing time inversions (TIs) of 50, 100, 200, 300, 450, 600, 750, 900, 1,100, 1500 and 1800 ms. The transverse nuclear relaxation times, *T*₂, were measured from axial *T*₂-weighted SE images obtained with a TR of 2000 ms and increasing TEs of 20, 40, 60, and 80 ms.

The thermogravimetric analysis (TGA) curves were recorded using a LabsSys evo TG-DTA-DSC 16000 device from Setaram Instrumentation.

The fluorescence measurements were performed with a Spex FluoroMax spectrofluorometer (HORIBA Jobin-Yvon, France) equipped with a Hamamatsu 928 photomultiplier.

Surface plasmon resonance measurements were carried out using a BIAcore X100 (GE Healthcare) with a sensor chip CM5 (GE Healthcare).

The ^{125}I echistatin radioactivity was counted in a gamma counter Wizard 1470 (Perkin Elmer).

Superparamagnetic nanoparticle preparation

Synthesis of $\gamma\text{Fe}_2\text{O}_3$ nanocrystals. The maghemite NPs, $\gamma\text{Fe}_2\text{O}_3$ nanocrystals^{24,25} (average diameter 9 nm and size distribution $\sigma = 0.2$, see ESI Fig. S1†) were synthesized according to the following procedure. Dimethylamine ($(\text{CH}_3)_2\text{NH}$) was added to an aqueous solution of ferrous dodecyl sulfate ($\text{Fe}(\text{DS})_2$). The final concentrations after the reactants mixed were $2.7 \times 10^{-2} \text{ mol L}^{-1}$ and $2.8 \times 10^{-1} \text{ mol L}^{-1}$ for $\text{Fe}(\text{DS})_2$ and dimethylamine, respectively. The solution was then stirred vigorously for 2 h at 28.5 °C. 2 mL of HCl (1 M) were then added, in order to reach the isoelectric point (around pH 7), inducing nanoparticle precipitation. The precipitate was isolated from the supernatant using magnetic separation. After 10 washings at neutral pH, the nanoparticles were then dispersed at pH 2 in distilled water. At this stage uncoated $\gamma\text{-Fe}_2\text{O}_3$ nanocrystals were produced.

Synthesis of $\gamma\text{Fe}_2\text{O}_3@CA$ nanocrystals. After synthesis, the nanoparticle surface was directly functionalized with caffeic acid. 10 mL of an aqueous caffeic acid solution (10 mg mL^{-1}) at pH 10 was directly mixed with 10 mL of bare $\gamma\text{-Fe}_2\text{O}_3$ particle suspension (6 mg mL^{-1}) at pH 10. After mixing for two hours at room temperature, the functionalized magnetic particles were washed 5 times using magnetic separation at pH 2. Then, the magnetic $\gamma\text{Fe}_2\text{O}_3@CA$ particles were dispersed in distilled water and adjusted to pH 7. The average number of molecules of CA per nanocrystal was measured by thermogravimetric analysis.

Coupling onto $\gamma\text{Fe}_2\text{O}_3@CA$ nanocrystals and characterization. In the following procedures, the coupling of the molecule (R123 dye, $\text{H}_2\text{N}-(\text{PEG})_4\text{-COOH}$ or cRGD derivatives) onto the caffeic acid functionalized maghemite was performed in water in a two-step procedure (activation and conjugation) at room temperature or assisted by microwaves (see ESI† for the comparison of coupling efficiency with and without microwaves). Firstly, the carboxylic acid functions at the outer surface of the nanocrystals were activated using 1-ethyl-3-(3-dimethylaminopropyl) carbodiimide (EDC, $n_{\text{EDC}} = 5n_{\text{COOH}}$) and *N*-hydroxysuccinimide (NHS, $n_{\text{NHS}} = 5n_{\text{COOH}}$) at pH 4. The second step was the linkage of the amine function of the interest molecule with the activated carboxylic acid functions on the nanocrystals. The pH of the $\gamma\text{Fe}_2\text{O}_3@CA$ ferrofluid was adjusted to 9 with *N,N*-diisopropylethylamine. The ligand was dissolved in water at pH 9 and then added to the ferrofluid.

The procedure was carried out with various molar ratios $R = n_{\text{COOH}}/n_{\text{NH}_2}$. The modified particles were isolated with a magnet at pH 2 and washed several times with deionized water. The particles were re-dispersed in water at physiological pH for various physicochemical characterizations.

The coupling efficiency of the dye R123 conjugation was investigated qualitatively using various measurement methods: infrared spectroscopy, dynamic light scattering, derivative

magnetization (Miaplex®), and quantitatively using fluorescence spectroscopy. The number of dyes per nanoparticle was determined after molecule desorption with an alkaline medium (pH 12 for 24 h) using a previously described procedure.²⁶ The magnetic particles were then separated from the supernatant by magnetic decantation. The pH of the supernatant was adjusted to physiological pH and the concentration of R123 was deduced from fluorescence measurements (see ESI Fig. S4†).

The average number of molecules of $\text{H}_2\text{N}-(\text{PEG})_4\text{-COOH}$ per nanocrystal was measured by several methods: infrared spectroscopy and OPA method. For the infrared spectroscopy method, infrared spectra in KBr pellets of various proportions of $\text{H}_2\text{N}-(\text{PEG})_4\text{-COOH}$ mixed with a constant amount of $\gamma\text{Fe}_2\text{O}_3@CA$ were recorded. Then, the normalized 1110 cm^{-1} band was used for the establishment of the calibration curve and the average number of $\text{H}_2\text{N}-(\text{PEG})_4\text{-COOH}$ per nanoparticle was deduced from this curve. For the OPA method, 50 μL of the sample was diluted in 50 μL of NaOH 2 N and left overnight at 60 °C. 1 mL of OPA reagent was added to the mixture and fluorescence measurement was recorded. The average number of $\text{H}_2\text{N}-(\text{PEG})_4\text{-COOH}$ per nanoparticle was deduced from a calibration curve (see ESI Fig. S6†).

The average number of cRGD derivatives was measured by the OPA method after calibration curve establishment (see ESI Fig. S10†).

MRI measurements. The ^1H NMR relaxometric characterization was performed by measuring the longitudinal relaxation times T_1 and the transverse nuclear relaxation times T_2 , on a 1.5 T MRI scanner. The measurements were performed at room temperature for various iron concentrations between 0.061 and 0.25 mM. The efficiency of MRI contrast agents was determined by measuring the relaxivity r_1 defined as $r_1 = (1/T_1)_{\text{meas}}/C$ and the relaxivity r_2 defined as $r_2 = (1/T_2)_{\text{meas}}/C$, where $(1/T_1)_{\text{meas}}$ or $(1/T_2)_{\text{meas}}$ was the value measured with the sample at concentration C of iron.

Biological stability. The biological stability of $\gamma\text{Fe}_2\text{O}_3@CA$ -R123 and $\gamma\text{Fe}_2\text{O}_3@CA\text{-PEG-R123}$ was evaluated by fluorescence spectroscopy using a previously described method.²⁷ Briefly, the particles were dispersed in 10% or 50% of FBS (Fetal Bovine Serum) at an iron concentration of 0.1 mM. The fluorescence intensity was recorded as a function of time.

$\alpha_v\beta_3$ targeting efficiency by surface plasmon resonance. Surface plasmon resonance measurements were used to investigate the efficiency of the interaction between the integrin $\alpha_v\beta_3$ and the cRGD derivatives coupled to $\gamma\text{Fe}_2\text{O}_3@CA$. The nanoparticles on the surface of carboxymethyl dextran (CMD)-coated gold were immobilized by electrostatic interactions. Briefly, the flow channel of BIAcore was equilibrated with Hepes buffer. The cRGD derivative nanoparticles were immobilized on the second channel of the sensor chip using a flow rate of $5 \mu\text{L min}^{-1}$ and the $\gamma\text{Fe}_2\text{O}_3@CA$ used as a reference was immobilized on the first channel. Integrin $\alpha_v\beta_3$ solutions were injected into the BIAcore flow channels at a flow rate of $30 \mu\text{L min}^{-1}$ and allowed to interact with the immobilized receptor. The specific interaction with the cRGD derivatives shifted the wavelength at which the surface plasmon resonance occurred. This shift was registered as response units (RU).

$\alpha_v\beta_3$ targeting efficiency by solid phase receptor binding assay. The receptor binding assay was performed as described previously.^{28,29} $\alpha_v\beta_3$ was diluted at 500 ng mL⁻¹ in coating buffer (20 mM tris, pH 7.4, 150 mM NaCl, 2 mM CaCl₂, 1 mM MgCl₂, 1 mM MnCl₂) and an aliquot of 100 μ L per well was added to a 96-well microtiter plate (Microlite 2+, Thermo Scientific) and incubated overnight at 4 °C. The plate was washed once with blocking/binding buffer (20 mM tris, pH 7.4, 150 mM NaCl, 2 mM CaCl₂, 1 mM MgCl₂, 1 mM MnCl₂, 1% bovine serum albumin) and incubated for an additional 2 h at room temperature. The plate was rinsed twice with the same buffer and incubated with the radiolabeled ligand at the indicated concentrations for 3 h at room temperature. For co-incubations, an unlabeled competitor was included at the concentrations described. After three additional washes with blocking/binding buffer, counts were obtained with boiling in 2 N NaOH and subjected to γ -counting. Non-specific binding of the ligand to the receptor was determined with molar excess (200-fold) of the unlabeled ligand. Each data point was a result of the average of triplicate wells.

Results and discussion

$\gamma\text{Fe}_2\text{O}_3$ @CA nanoplatform

Infrared spectroscopy is a very useful and direct technique for studying the nature of surface complexation functions. Catechol and carboxylic groups are well known as highly chelating agents for the metal oxide surface. The CA coating on $\gamma\text{Fe}_2\text{O}_3$ NPs caused major changes in the spectra compared to free CA (Fig. 1).

The infrared spectra of free CA (red curve, Fig. 1) is characterized by different vibration bands (i) the alkene C=C stretching vibration band at 1639 cm⁻¹, (ii) the aromatic ring C=C stretching vibration bands at 1602 and 1522 cm⁻¹, (iii) the stretching vibrations of the phenolic group C-OH at 1417, 1376 and 978 cm⁻¹ and bending vibrations of the phenolic group C-OH at 1280, 1522 and 1117 cm⁻¹ and (iv) the stretching and/or bending vibration of CO or OH in COOH at 1293, 1208 and 1163 cm⁻¹.^{30,31} Upon adsorption of CA onto $\gamma\text{Fe}_2\text{O}_3$ NPs (green curve, Fig. 1) the difference between infrared spectra of free and adsorbed CA appears, indicating surface complexation with catechol bound to the oxide surface *via* two adjacent phenolic

groups. The most notable modification on an IR spectrum of $\gamma\text{Fe}_2\text{O}_3$ @CA, in addition to the appearance of a strong Fe-O stretching vibration band at 600 cm⁻¹ (inset Fig. 1), is the complete disappearance of the bands at 978 cm⁻¹, the decrease of the intensity band at 1417 cm⁻¹, while the band at 1280 cm⁻¹ shift to 1267 cm⁻¹. These bands, assigned to stretching and bending vibrations of phenolic OH groups, are likely those participating in the nanoparticle surface complexation with catechol bound to the oxide surface in a bidentate form (Fig. 1B). The binding of CA to iron oxide even affects the stretching of the aromatic ring (bands > 1400 cm⁻¹). The most noticeable is the appearance of the strong characteristic band of a conjugated aromatic ketone (\sim 1605 cm⁻¹),³² which confirms the bidentate bonding of the catechol to the surface of the nanoparticles.

Similar results were obtained on various nanocrystalline metal oxides such as TiO₂, Fe₂O₃, Fe₃O₄ and ZrO₂, surface functionalized with various enediol ligands³³⁻³⁵ and with 5-hydroxy-5,5-bis(phosphono)pentanoic acid onto $\gamma\text{Fe}_2\text{O}_3$ NPs:²⁴ the interaction with the surface takes place through the hydroxymethylene bisphosphonate group, and the pendant carboxylate is free and exposed to solution.

Hence, adding CA results in the replacement of nanoparticle surface OH groups and the coordination of surface Fe atoms with both OH groups of catechol.

The average number of CA molecules was deduced using thermogravimetric analysis and was found to be of 1100 per nanoparticle which corresponds to a surface area of 23.1 Å² occupied by each CA ligand molecule (see ESI, Fig. S2†). This surface area is comparable to the results obtained on surface modification of anatase particles with dopamine ligands.³⁶

The $\gamma\text{Fe}_2\text{O}_3$ @CA NPs formed highly stable ferrofluid in a large range of pH, from pH 4 to pH 11 (Fig. 2A). At physiological pH, the hydrodynamic diameter and zeta potential surface are found equal to 12.5 nm and -45 ± 5 mV respectively. Considering the mean crystalline core (9 nm in diameter) and a layer of about 0.9 nm for the coating of CA molecules,³⁷ this suggested very low aggregation.

Concerning magnetic measurements, the magnetization curve (Fig. 2B) and the second derivative of magnetization (inset Fig. 2B, measured with MIAplex® detector) are characteristic of superparamagnetic behavior. It has to be noticed that 11 months after synthesis no decomposition of the iron oxide NPs and consequently alteration of the magnetic properties has been observed (see ESI Fig. S3†). The degradation of iron oxide nanoparticles has been reported for other catechol derivatives such as dopamine.^{32,38} Caffeic acid can be compared to nitrodopamine, another catechol derivative, which has irreversible high affinity binding under physiologic conditions.³⁹ Indeed the terminal conjugated COOH group from caffeic acid is a high electron withdrawing group as the NO₂ group from nitrodopamine.

Once these nanoparticles $\gamma\text{Fe}_2\text{O}_3$ @CA characterized, the carboxylic acid functions at the outer surface were then used for the covalent coupling of different ligands (R123, H₂N-(PEG)₄-COOH or cRGD derivatives) using carbodiimide chemistry with a microwave assisted procedure. We recently showed that in the

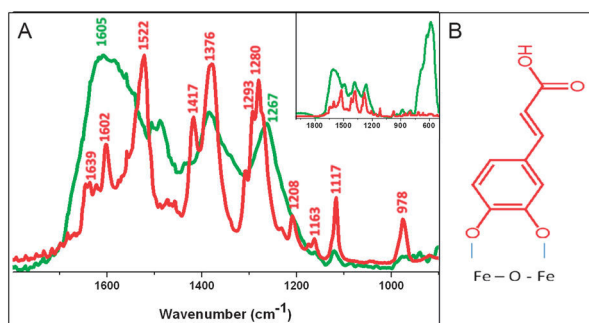


Fig. 1 (A) IR spectra of CA (red) and $\gamma\text{Fe}_2\text{O}_3$ @CA (green); (B) coordination mode of iron surface NPs with a catechol complex.

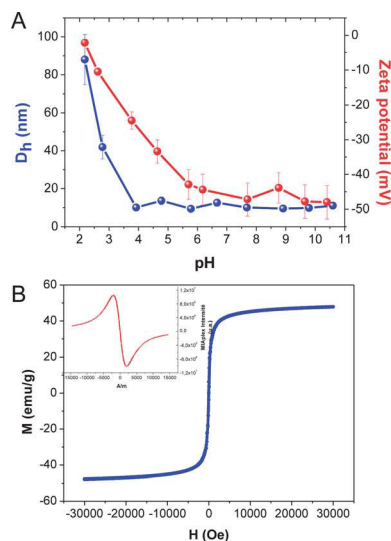


Fig. 2 (A) Hydrodynamic diameter (blue) and zeta potential (red) of $\gamma\text{Fe}_2\text{O}_3@CA$; (B) the $\gamma\text{Fe}_2\text{O}_3@CA$ magnetization curve and the second derivative of magnetization in the inset.

case of amide bond formation, the functionalization yield could be increased using micro-wave energy.²⁶ As described above, the ultimate goal is to obtain a multimodal nanoplatform. Our approach was to study each coupling and then various combinations to optimize the nanosystem.

Coupling efficiency study on a $\gamma\text{Fe}_2\text{O}_3@CA$ nanoplatform

Dye R123 coupling: $\gamma\text{Fe}_2\text{O}_3@CA-R123$. For the dye R123 coupling onto a $\gamma\text{Fe}_2\text{O}_3@CA$ nanoplatform, microwave conditions were used. High coverage of the surface of the NPs by R123 was obtained by this method²⁶ as demonstrated by infrared, UV-Visible and fluorescence spectroscopies (see ESI Table S1† for comparison of conventional *versus* microwave covalent coupling). The microwave treatment conditions have been defined to $t_{\text{max}} = 3$ min and $T_{\text{max}} = 150$ °C. Several molar ratios for R123 *versus* COOH functions were tested ($R = n_{R123}/n_{COOH}$).

Fig. 3A shows the infrared spectra of the nanoplatform $\gamma\text{Fe}_2\text{O}_3@CA$ (green curve), R123 (pink curve) and after coupling corresponding to $R = 2$ (blue curve) and $R = 20$ (black curve).

For a low ratio ($R = 2$), the infrared spectrum (blue curve) is very similar to the native nanoplatform $\gamma\text{Fe}_2\text{O}_3@CA$ (green curve) whereas increasing the molar ratio to $R = 20$ (black curve) leads to large changes all over the spectrum range suggesting successful tailoring of the nanoparticle surface with R123 (Fig. 3A). The characteristic vibration bands of the functionalized nanoparticles Fe–O (600 cm^{-1}), C–O (1267 cm^{-1}), as well as R123 (between 1000 and 1800 cm^{-1}) appeared on the spectrum, indicating efficient binding of R123 onto the nanoparticle surface. A new band appears around 1634 cm^{-1} arising from the amide bonding between R123 and $\gamma\text{Fe}_2\text{O}_3@CA$ nanocrystals which shows the successful derivatization of carboxylic acid at the outer surface with the amine group of R123.

Similar to infrared characterization, the efficiency of R123 coupling on a nanoplatform is only detectable for a ratio $R = 20$

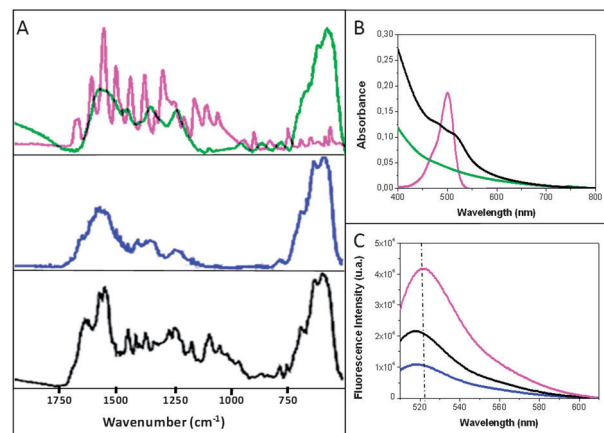


Fig. 3 (A) IR spectra of $\gamma\text{Fe}_2\text{O}_3@CA$ (green curve), free R123 (pink curve) and $\gamma\text{Fe}_2\text{O}_3@CA-R123$ $R = 2$ (blue curve) and $R = 20$ (black curve); (B) absorption spectra of free R123 (pink curve $C = 3 \times 10^{-6}$ M), $\gamma\text{Fe}_2\text{O}_3@CA$ (green curve $C_{Fe} = 1.2 \times 10^{-4}$ M) and $\gamma\text{Fe}_2\text{O}_3@CA-R123$ $R = 20$ (black curve $C_{Fe} = 2.9 \times 10^{-4}$ M); (C) emission fluorescence spectra ($\lambda_{\text{exc}} = 500$ nm) of $\gamma\text{Fe}_2\text{O}_3@CA-R123$ $C_{Fe} = 2 \times 10^{-4}$ M, $R = 2$ (blue) and $R = 20$ (black) before (blue) and after R123 desorption (pink) ($R = n_{R123}/n_{COOH}$).

with UV-Visible spectroscopy (Fig. 3B). Under this condition, a small bump around 520 nm appears due to grafting of R123 onto the NP surface, which is red-shifted compared to free R123 (500 nm). Successful grafting is highlighted by emission fluorescence spectroscopy. The fluorescence emission spectrum of the $\gamma\text{Fe}_2\text{O}_3@CA-R123$ gave a maximum wavelength at 518 nm, slightly blue-shifted compared to free R123 (around 4 nm), Fig. 3C.

The fluorescence emission intensity increases with the ratio R , due to the large number of R123 grafted onto the NP surface. It is well known that quenching occurs due to both an energy transfer process between the iron oxide and the fluorophore and intermolecular quenching.^{25,40–42} The average number of rhodamine per nanoparticle, quenching factor and yield coupling are reported in Table 1. These values are deduced after a 24 h treatment of $\gamma\text{Fe}_2\text{O}_3@CA-R123$ ferrofluid in an alkaline medium. Under this condition the coating is removed from the surface of the nanoparticles and the supernatant is titrated by fluorescence.²⁵ Hence increasing the ratio R increases the average number of R123 per nanoparticle and the emission is decreased by a factor 5 (Table 1).

Dynamic light scattering also revealed that the efficiency of coupling is correlated with the excess of R123 (ratio R). Compared to $\gamma\text{Fe}_2\text{O}_3@CA$ nanocrystals, the synthesized fluorescent particles with a constant zeta potential displayed an increase of the mean hydrodynamic diameter (see Table 1). Increasing the number of R123 molecules per nanoparticle favours steric hindrance as well as π - π stacking between R123 of neighboring nanoparticles and induces aggregation states. Magnetic measurements show that superparamagnetic behavior is maintained for these R ratios (see ESI, Fig. S5†).

$\text{H}_2\text{N}-(\text{PEG})_4-\text{COOH}$ coupling: $\gamma\text{Fe}_2\text{O}_3@CA-\text{PEG}-\text{COOH}$. In order to covalently link PEG chains on the $\gamma\text{Fe}_2\text{O}_3@CA$ nanoplatform, the approach, described for dye coupling, was applied using $\text{H}_2\text{N}-(\text{PEG})_4-\text{COOH}$. Several stoichiometric ratios were tested ($R = n_{\text{PEG}}/n_{\text{COOH}}$) under microwaves.

Table 1 R123 molecule number before and after molecule desorption, quenching and percentage of R123 per nanoparticle for $R = 2$ and $R = 20$, and dynamic light scattering properties (hydrodynamic size, polydispersity index, and zeta potential)

	R	Grafted molecule number		Quenching	%	D_h (nm)	Pdi	Zeta (mV)
		Before and after desorption						
R123	0	—		—	0	12.5	0.2	-45 ± 5
	2	3 ± 1	11 ± 3	4	1 ± 0.3	24.2	0.3	-44 ± 7
	20	11 ± 1	55 ± 1	5	5 ± 0.1	32.2	0.3	-41 ± 10

With the aim of quantifying coupling efficiency by infrared spectroscopy, $\gamma\text{Fe}_2\text{O}_3@CA$ nanoplateforms were mixed with various amounts of free $\text{H}_2\text{N}-(\text{PEG})_4-\text{COOH}$. Comparing the overlapping of $\gamma\text{Fe}_2\text{O}_3@CA$ and $\text{H}_2\text{N}-(\text{PEG})_4-\text{COOH}$ IR spectra (Fig. 4A), the sharp band at 1110 cm^{-1} corresponding to C–O symmetric stretching of $\text{H}_2\text{N}-(\text{PEG})_4-\text{COOH}$ could be used for quantification. Indeed, a linear relationship of the C–O band area, normalized with the Fe–O vibration band (from 500 to 750 cm^{-1}) was obtained by increasing the amount of free $\text{H}_2\text{N}-(\text{PEG})_4-\text{COOH}$ (Fig. 4B and the inset).

The spectra of the composite nanoparticles $\gamma\text{Fe}_2\text{O}_3@CA\text{-PEG-COOH}$ (Fig. 4C) are similar to those of pure PEG and $\gamma\text{Fe}_2\text{O}_3@CA$ nanoplateforms, respectively. An increase in the average number of PEG grafted onto the nanoparticle surface with the R ratio is observed, corresponding to an increase of coverage yield from 6% to 15% (Table 2).

To check our quantitative infrared assay, OPA and thermogravimetric analysis methods were also used. The OPA^{43,44} reacts with amines to form blue fluorescent isoindoles in the presence of reduced thiols.^{45,46} This reagent is not only used for assays of amino groups, but also for assays of thiol groups.^{47,48} The amount of grafted $\text{H}_2\text{N}-(\text{PEG})_4-\text{COOH}$ per nanoparticle is deduced after chemical decomposition (2 N NaOH, $60\text{ }^\circ\text{C}$, overnight) of the coupling and titration of amino groups in the supernatant. A range of concentrations of free $\text{H}_2\text{N}-(\text{PEG})_4-\text{COOH}$ solutions ($50\text{ }\mu\text{L}$) added with basic solution ($50\text{ }\mu\text{L}$, 2N NaOH, $60\text{ }^\circ\text{C}$, overnight) were prepared for calibration (see ESI, Fig. S6†). The coverage yields for various ratios R are reported in Table 2. Thermogravimetric analysis was performed only for one sample corresponding to ratio $R = 5$ (see ESI Fig. S7†) and a coverage yield of $9 \pm 3\%$ was measured.

A good correlation is obtained by comparing the results deduced with IR spectroscopy, thermogravimetric analysis and OPA methods (Table 2). This validates our IR approach for PEG quantification after covalent coupling on $\gamma\text{Fe}_2\text{O}_3@CA$ nanoplateforms. A major advantage of the latter method is the lower consumption of material as compared to thermogravimetric analysis (only 10 mg of material is needed) or OPA (the reagent is unstable and sensitive to storage conditions which increases the work and the costs, if the new reagent solution needs to be prepared for each quantification).

The hydrodynamic size and zeta potential of $\gamma\text{Fe}_2\text{O}_3@CA\text{-PEG-COOH}$ are similar to the $\gamma\text{Fe}_2\text{O}_3@CA$ nanoplateform. The results are consistent with the low $\text{H}_2\text{N}-(\text{PEG})_4-\text{COOH}$ coverage yield (15% maximum) and to the fact that the

carboxylic acid function on the $\gamma\text{Fe}_2\text{O}_3@CA$ nanoplateform used for the covalent coupling is substituted to the carboxylic acid function of the conjugated PEG. This induced no charge surface modification.

It has to be noticed that with the same experimental conditions, the coupling yield on the $\gamma\text{Fe}_2\text{O}_3@CA$ nanoplateform is higher for PEG (6–15%) compared to R123 (1–5%). This effect could be correlated with higher amine reactivity and lower steric hindrance with $\text{H}_2\text{N}-(\text{PEG})_4-\text{COOH}$ compared to R123.

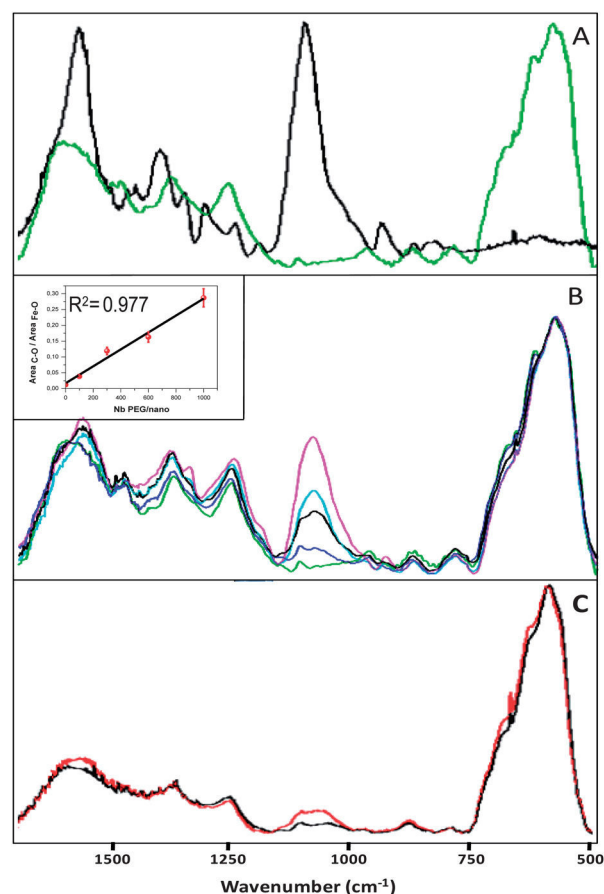


Fig. 4 IR spectra of (A) $\gamma\text{Fe}_2\text{O}_3@CA$ (green) and PEG (black); (B) $\gamma\text{Fe}_2\text{O}_3@CA$ and $\text{H}_2\text{N}-(\text{PEG})_4-\text{COOH}$ mixed in various proportions corresponding to a number of PEG per nanoparticle equal to 100 (dark blue), 300 (black), 600 (blue), and 1000 (pink) – linear increase of the C–O band area (normalized with the Fe–O band) with the number of PEG in the inset; (C) $\gamma\text{Fe}_2\text{O}_3@CA\text{-PEG-COOH}$ $R = 2$ (blue), $R = 5$ (pink), $R = 20$ (black) and $R = 50$ (red), ($R = n_{\text{PEG}}/n_{\text{COOH}}$).

Table 2 H₂N-(PEG)₄-COOH number and percentage per nanoparticle for various ratios ($R = n_{\text{PEG}}/n_{\text{COOH}}$) deduced from infrared spectroscopy and OPA reagent methods, and dynamic light scattering properties (hydrodynamic size, polydispersity index, and zeta potential)

	R	Grafted molecule number				D_h (nm)	Pdi	Zeta (mV)
		IR	%	OPA	%			
PEG	2	68 ± 7	6 ± 1	88 ± 13	8 ± 1	11.8	0.3	-41 ± 7
	5	70 ± 8	6 ± 1	80 ± 20	7 ± 2	9.2	0.3	-41 ± 7
	20	140 ± 15	13 ± 1	120 ± 6	11 ± 1	17.7	0.3	-34 ± 9
	50	170 ± 18	15 ± 2	142 ± 7	13 ± 1	11.6	0.3	-47 ± 7

cRGD derivative coupling: $\gamma\text{Fe}_2\text{O}_3@CA\text{-cRGD}$ and $\gamma\text{Fe}_2\text{O}_3@CA\text{-(PEG-cRGD)}$. The lysine residue (K) of c(RGDfK) or the amine function of c(RGDfK)-PEG₂-NH₂ was used to covalently link cRGD derivatives on the $\gamma\text{Fe}_2\text{O}_3@CA$ nanoplatfom, under microwaves. The microwave treatment conditions have been set to $t_{\text{max}} = 3$ min and $T_{\text{max}} = 65$ °C. Indeed, the structure and properties of biomolecules such as peptides or proteins are very sensitive to time and temperature. The infrared spectra of c(RGDfK) before and after this microwave treatment show no modification, suggesting the stability of the cyclic peptide under microwaves (see ESI, Fig. S8†). The coupling procedures were applied for various ratios ($R_{\text{cRGD}} = n_{\text{cRGD}}/n_{\text{COOH}}$). Compared to the $\gamma\text{Fe}_2\text{O}_3@CA$ nanoplatfom, the infrared spectra after cRGD derivative coupling show no evidence of efficient conjugation (see ESI Fig. S9†). As highlighted with the OPA assay (below), this is due to the weak coverage yield. The amount of cRGD ligand grafted per nanoparticle was deduced using the OPA method (Table 3).

As observed previously for dye and H₂N-(PEG)₄-COOH coupling, the coupling enhancement increases with the ratio R . The coverage yield is lower using c(RGDfK) compared to c(RGDfK)-PEG₂-NH₂. The cRGDfK steric hindrance is reduced by the presence of PEG linkers.

DLS measurements (Table 3) indicate that for a same number of cRGD per nanoparticle the hydrodynamic size is largest for $\gamma\text{Fe}_2\text{O}_3@CA\text{-PEG-cRGD}$ than $\gamma\text{Fe}_2\text{O}_3@CA\text{-cRGD}$ in accordance with the increase of coverage yield.

Finally, comparing H₂N-(PEG)₄-COOH and c(RGDfK)-PEG₂-NH₂ coupling, for the same R value ($R = 2$ and 20, Tables 2 and 3), the coverage yield is similar.

Toward multimodal nanoplatfom. To implement the functionalization of the $\gamma\text{Fe}_2\text{O}_3@CA$ nanoplatfom with R123, H₂N-(PEG)₄-COOH and cRGD derivatives, different moieties were

sequentially introduced by successive carboxyl group activation. The cRGD peptide presenting carboxyl groups in the aspartic acid side chain is introduced in the last step.

First, we studied the 2 step functionalization with R123 and H₂N-(PEG)₄-COOH using $\gamma\text{Fe}_2\text{O}_3@CA\text{-PEG-COOH}$ and $\gamma\text{Fe}_2\text{O}_3@CA\text{-R123}$ nanoplatfoms respectively. The average number of grafted molecules is reported in Table 4. It can be observed that the second step surface functionalization induces lower coverage efficiency as compared to the two nanoplatfoms.

Moreover after addition of H₂N-(PEG)₄-COOH ($R = 50$) onto the $\gamma\text{Fe}_2\text{O}_3@CA\text{-R123}$ nanoplatfom, an increase of fluorescence quenching factor from 4 to 7 was observed (Table 5). The same quenching factor was obtained after grafting R123 ($R = 2$) onto the $\gamma\text{Fe}_2\text{O}_3@CA\text{-PEG-COOH}$ nanoplatfom. DLS measurements performed before and after the second step surface functionalization show an increase of hydrodynamic diameter and decrease of zeta potential. This indicates that some aggregation occurs during the second step that could explain the increase of quenching factor due to intermolecular quenching.²⁶ Considering R123 coupling on the $\gamma\text{Fe}_2\text{O}_3@CA\text{-PEG-COOH}$ nanoplatfom, the dye could be linked with COOH of CA (around 960) or PEG chains (142). In the latter case, a decrease of quenching factor due to the PEG linker spacer could be expected by decreasing the dye-NP surface interaction. This suggests that R123 coupling occurs with COOH of CA.

The coupling efficiency of c(RGDfK)-PEG₂-NH₂ ($R = 2$) is similar compared to the coupling on the $\gamma\text{Fe}_2\text{O}_3@CA\text{-R123}$ nanoplatfom (two step functionalization, 64 c(RGDfK)-PEG₂-NH₂, Table 4) with the $\gamma\text{Fe}_2\text{O}_3@CA$ nanoplatfom (one step functionalization, 61 c(RGDfK)-PEG₂-NH₂, Table 3). The same quantity of cRGDfK was calculated with the three step functionalization consisting in sequential addition of R123 ($R = 2$),

Table 3 c(RGDfK) and c(RGDfK)-PEG₂-NH₂ numbers and percentage per nanoparticle for various ratios ($R = n_{\text{cRGD}}/n_{\text{COOH}}$) deduced with the OPA reagent method, and dynamic light scattering properties (hydrodynamic size, polydispersity index, and zeta potential)

	R	Grafted molecule number		D_h (nm)	Pdi	Zeta (mV)
		OPA	%			
cRGDfK	0.2	25 ± 2	2 ± 0.2	16	0.3	-44 ± 12
	2	43 ± 4	4 ± 0.4	18	0.2	-43 ± 12
	20	59 ± 9	5 ± 1	15	0.3	-44 ± 8
c(RGDfK)-PEG ₂ -NH ₂	0.2	35 ± 8	3 ± 1	22	0.3	-36 ± 12
	2	61 ± 3	6 ± 0.3	18	0.2	-39 ± 7
	20	130 ± 30	12 ± 3	30	0.3	-40 ± 10

Table 4 R123, H₂N-(PEG)₄-COOH and cRGD ligand number and % per multimodal nanoplatform and fluorescence imaging

Grafted molecule order			Grafted molecule number							
1 st	2 nd	3 rd	R123	% R123	Fluorescence image	PEG	% PEG	cRGD	% cRGD	
PEG	R123	—	8 ± 1	0.7 ± 0.1	●	142 ± 7	13 ± 0.6	—	—	
R123	PEG	—	11 ± 2	1 ± 0.2	●	93 ± 11	8 ± 1	—	—	
R123	cRGDfk-PEG ₂ -NH ₂	—	11 ± 2	1 ± 0.2	●	64 ± 1	3 ± 0.2	64 ± 1	6 ± 0.1	
R123	PEG	cRGDfk	11 ± 2	1 ± 0.2	●	93 ± 11	8 ± 1	62 ± 5	6 ± 0.5	

Table 5 Quenching and dynamic light scattering properties (hydrodynamic size, polydispersity index, and zeta potential) of the multimodal nanoplatforms

Grafted molecule order			Quenching		D _h (nm)		Pdi		Zeta (mV)	
1 st	2 nd	3 rd	Before	After	Before	After	Before	After	Before	After
PEG	R123	—	—	7	12	31	0.3	0.3	-47 ± 7	-37 ± 6
R123	PEG	—	4	7	24	34	0.3	0.3	-44 ± 7	-41 ± 11
R123	cRGDfk-PEG ₂ -NH ₂	—	4	32	24	35	0.3	0.2	-44 ± 7	-44 ± 6
R123	PEG	cRGDfk	7	29	34	37	0.3	0.3	-41 ± 11	-33 ± 7

then H₂N-(PEG)₄-COOH ($R = 50$) and finally cRGDfk ($R = 2$) (Table 4). Comparing these two methods, similar number of dye, PEG chains and cRGD ligands were obtained with comparable dynamic light scattering properties (Table 5). However the two step functionalization is less time consuming. In addition, the R123 quenching increases drastically, but is still sufficient for fluorescence imaging as shown in Table 4.

The surface functionalization of the $\gamma\text{Fe}_2\text{O}_3@CA$ nanoplatform with R123, H₂N-(PEG)₄-COOH and cRGD derivatives was successfully performed and characterized. To complete this study, the stability of these nanoplatforms in the biological environment was performed, and their properties as MRI contrast agents as well as their affinity towards integrins were evaluated.

Biological stability

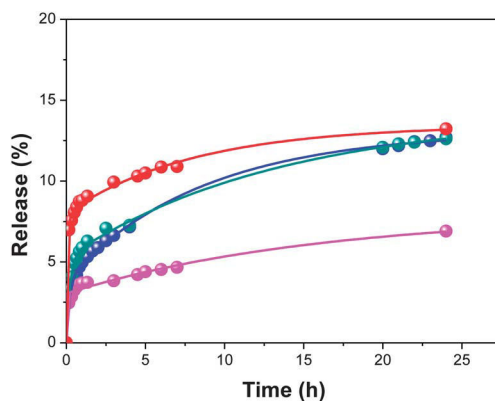
NP stability in serum is an important criterion for their utility as target nanosystems *in vivo*. Using the change in fluorescence emission intensity in the presence of plasma as a surrogate for protein adsorption, stability in the serum of $\gamma\text{Fe}_2\text{O}_3@CA$ -R123 and $\gamma\text{Fe}_2\text{O}_3@CA$ -PEG-R123 nanoplatforms was studied. Nanoplatforms were incubated with 10% and 50% FBS (Fetal Bovine Serum) solutions. The kinetic displacement of the quenched and bound R123 on the NP surface was monitored by fluorescence spectroscopy. The quenching factor in serum is similar to that measured in water (see ESI Table S2†). After 24 h, less than 15% of release is reached, (Fig. 5). This evidenced the bio-stability of this nanoplatform through the high CA anchoring on the iron oxide surface and the covalent coupling through amide binding. This argues the possibility of their use for *in vivo* experiments.

MRI analysis

Medical imaging techniques such as positron emission tomography (PET) and magnetic resonance imaging (MRI) are

routinely used in hospitals and allow detection of pathological tissues such as cancer. In comparison with PET, MRI is a very powerful imaging tool due to its high spatial resolution. However, a major limitation of MRI is the low sensitivity to exogenous molecular probes (contrast agents). The next generation of dual-modality instruments based on the combination of PET and MRI could become promising.⁴⁹⁻⁵² Another approach is to engineer the properties of the MRI probe to optimize its sensitivity. To examine the feasibility of the as-synthesized nanoparticles as MRI contrast agent, the relaxation times T_1 and T_2 were measured on a 1.5T clinical MR scanner at room temperature for various iron concentrations. The longitudinal r_1 relaxivity is deduced from T_1 -weighted images obtained from an inversion recovery sequence. The transverse nuclear relaxation times, T_2 , were measured from a spin echo sequence.

As shown in Fig. 6A and B, T_1 and T_2 weighted images of the $\gamma\text{Fe}_2\text{O}_3@CA$ nanoplatform change in signal intensity with an increasing amount of nanoparticles, indicating that the

**Fig. 5** Release of $\gamma\text{Fe}_2\text{O}_3@CA$ -R123 in 10% (pink) and 50% (red) FBS and release of $\gamma\text{Fe}_2\text{O}_3@CA$ -PEG-R123 in 10% (blue) and 50% (green) FBS.

synthesized nanoparticles generated MR contrast on proton relaxation times weighted sequences. As expected, relaxation rates varied linearly with the iron concentration (see ESI Fig. S11†). The longitudinal and transverse relaxivities (r_1 and r_2) were deduced from the slope of the curves and were $9(\pm 2)$ and $233(\pm 7)$ $\text{mM}^{-1} \text{s}^{-1}$ respectively. The high r_2/r_1 relaxivity ratio of 25.9 suggests a high T_2 -effect. This demonstrates that $\gamma\text{Fe}_2\text{O}_3@CA$ nanoparticles can be efficient T_2 contrast agents.

Fig. 6C shows the relaxivities r_2 for different synthesized nanoplateforms. r_2 constants varied from 185 up to 242 $\text{mM}^{-1} \text{s}^{-1}$, depending on their functionalization. This evidenced that the r_2 value is not too sensitive to the functionalization of the particle by small molecules. Moreover these r_2 values are slightly higher than commercial MRI contrasts agents such as the Endorem® from Guerbet ($98 \text{mM}^{-1} \text{s}^{-1}$) and the Resovist® from Bayer Healthcare ($151 \text{mM}^{-1} \text{s}^{-1}$).⁵³ Such values for r_2 suggest that CA coated nanoparticles can act as T_2 contrast agents due to their r_2 value.

Binding investigation

Surface plasmon resonance evaluation of interaction between various nanoplateforms with $\alpha_v\beta_3$ integrins. The availability of the cRGD ligand on the nanoparticles was first investigated using surface plasmon resonance. SPR is a very sensitive technique to study biomolecular events in the nanomolar range. In a first series of experiments, the CMD sensor chip was coupled with $\alpha_v\beta_3$ by the amine groups. To ensure a low non-specific binding of the nanoplateforms $\gamma\text{Fe}_2\text{O}_3@CA$

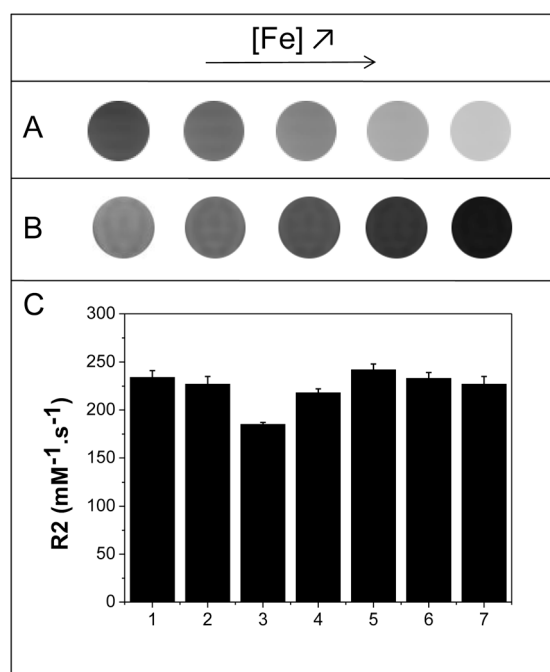


Fig. 6 (A) T_1 weighted ($TR = 2000$ ms, $TE = 16$ ms, $TI = 200$ ms) and (B) T_2 weighted ($TR = 2000$ ms, $TE = 20$ ms) MR images of $\gamma\text{Fe}_2\text{O}_3@CA$ at $C_{\text{Fe}} = 0.061$; 0.093; 0.125; 0.188; 0.25 mM; (C) r_2 relaxivity values of various nanoplateforms (1) $\gamma\text{Fe}_2\text{O}_3@CA$; (2) $\gamma\text{Fe}_2\text{O}_3@CA\text{-R123}$ $R = 2$; (3) $\gamma\text{Fe}_2\text{O}_3@CA\text{-PEG-COOH}$ $R = 50$; (4) $\gamma\text{Fe}_2\text{O}_3@CA\text{-cRGD}$ $R = 2$; (5) $\gamma\text{Fe}_2\text{O}_3@CA\text{-PEG-cRGD}$ $R = 2$; multimodal nanoplateforms (6) 2 step and (7) 3 step strategy.

nanoparticles were used as a blank. The nanoparticles were injected into the SPR instrument containing the $\alpha_v\beta_3$ -coated sensor chip. After injection, an immediate change in response was observed indicating a non-specific binding. In order to study the potential affinity, the previous standard procedure was changed, using the direct immobilization of nanoplateforms on CMD.

Fig. 7 shows the sensorgram of time depending on the binding of various nanoplateforms $\gamma\text{Fe}_2\text{O}_3@CA$, $\gamma\text{Fe}_2\text{O}_3@CA\text{-cRGD}$ ($R = 2$, 43 cRGDfK/NP) and $\gamma\text{Fe}_2\text{O}_3@CA\text{-PEG-cRGD}$ ($R = 2$, 61 c(RGDfK)-PEG₂-NH₂/NP) to the CMD coated surface of the Biacore chip.

The response values (RU) for $\gamma\text{Fe}_2\text{O}_3@CA$ (black curve Fig. 7A) and $\gamma\text{Fe}_2\text{O}_3@CA\text{-cRGD}$ (green curve Fig. 7A) are high, 1500 and 1800 respectively, indicating a strong interaction between these nanoplateforms and CMD. The RU signal is lower with the $\gamma\text{Fe}_2\text{O}_3@CA\text{-PEG-cRGD}$ nanoplateform (red curve Fig. 7A) and increases to 230 after 3 injections. It has to be noticed that despite various washings and drastic procedures

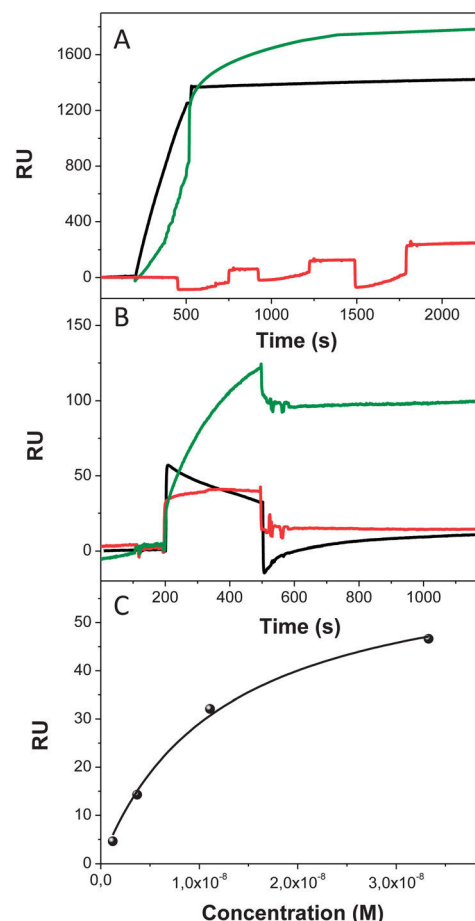


Fig. 7 (A) Immobilization of $\gamma\text{Fe}_2\text{O}_3@CA$ (black), $\gamma\text{Fe}_2\text{O}_3@CA\text{-cRGD}$ (green) and $\gamma\text{Fe}_2\text{O}_3@CA\text{-PEG-cRGD}$ (red, after 3 injections of $\gamma\text{Fe}_2\text{O}_3@CA\text{-PEG-cRGD}$) in order to increase the immobilization onto the CMD chip and (B) response after $\alpha_v\beta_3$ injection of 200 nM on $\gamma\text{Fe}_2\text{O}_3@CA$ (black), 1 nM on $\gamma\text{Fe}_2\text{O}_3@CA\text{-cRGD}$ (green, $R = 2$) and 30 nM on $\gamma\text{Fe}_2\text{O}_3@CA\text{-PEG-cRGD}$, $R = 2$ (red). (C) Steady state affinity of successive growing $\alpha_v\beta_3$ concentrations (1.23 nM, 3.7 nM, 11.1 nM and 33 nM) injected on $\gamma\text{Fe}_2\text{O}_3@CA\text{-cRGD}$.

tested using NaOH or HCl (100 nM), following the interaction phase, the constant signal demonstrates a strong interaction between these nanoplatforms and CMD. Such interaction could be due to the formation of hydrogen bonds between the large number of hydroxyl groups of CA (1100) and CMD. The interaction is largely switched off by the introduction of the c(RGDfK)-PEG₂-NH₂ spacer that reduces hydrogen bonding, resulting in a significant decrease of the signal. Fig. 7B shows the response of various nanoplatforms after $\alpha_v\beta_3$ injection, using each nanoplatform as a negative control (reference) on the first channel. The RU signal is nearly constant for the $\gamma\text{Fe}_2\text{O}_3\text{@CA}$ nanoplatform (black curve Fig. 7B) indicating no affinity with $\alpha_v\beta_3$ integrins. The RU signal increases for the other two nanoplatforms, going from $\gamma\text{Fe}_2\text{O}_3\text{@CA-(PEG-cRGD)}$ (RU = 14, red curve Fig. 7B) to $\gamma\text{Fe}_2\text{O}_3\text{@CA-cRGD}$ (RU = 100, green curve Fig. 7B) nanoplatforms, indicating increasing efficient binding.

Assuming the molecular weight of 150 kDa for integrin $\alpha_v\beta_3$ and around 1300 kg mol⁻¹ for immobilized nanoparticles the theoretical $\alpha_v\beta_3$ binding capacity (see ESI† SPR analysis) is around 25 RU and 200 RU for $\gamma\text{Fe}_2\text{O}_3\text{@CA-(PEG-cRGD)}$ and $\gamma\text{Fe}_2\text{O}_3\text{@CA-cRGD}$ nanoplatforms respectively. These values are in rather good agreement with experimental ones. It is worth mentioning that below 30 nM of $\alpha_v\beta_3$ concentration injection, no significant surface plasmon resonance signal change was observed with the $\gamma\text{Fe}_2\text{O}_3\text{@CA-(PEG-cRGD)}$ nanoplatform modified SPR chip surface. These results could be explained by taking into account the lower interaction of $\gamma\text{Fe}_2\text{O}_3\text{@CA-(PEG-cRGD)}$ compared to $\gamma\text{Fe}_2\text{O}_3\text{@CA-cRGD}$ nanoplatforms with a CMD chip.

A significant surface plasmon resonance binding kinetic assay was obtained after injection of various concentrations of $\alpha_v\beta_3$ over the $\gamma\text{Fe}_2\text{O}_3\text{@CA-cRGD}$ nanoplatform modified SPR chip surface (Fig. 7C). An affinity constant of 9 nM is deduced from steady state affinity. This value is several orders lower than the affinity constant of free cRGDfK published in the literature, 1.3 μM ,⁵⁴ suggesting a much better affinity of cRGDfK conjugated to the nanoplatform. Such difference could be due to a multivalence effect induced by the large number of cRGDfK grafted onto the $\gamma\text{Fe}_2\text{O}_3\text{@CA}$ nanoplatform.

Competition binding assay for $\alpha_v\beta_3$ integrin affinity. To determine the affinity and specificity of our various nanoplatforms to $\alpha_v\beta_3$ integrins, radioactive ¹²⁵I-labeled echistatin solid phase binding assay was used.²⁹ A purified $\alpha_v\beta_3$ receptor was coated on Microlite-2+ plates at a concentration of 50 ng per well as described in Materials and methods. ¹²⁵I-Echistatin was added to the wells to a final concentration of 0.05 nM in the presence of various competing ligands. cRGDfK, c(RGDfK)-PEG₂-NH₂ peptides and $\gamma\text{Fe}_2\text{O}_3\text{@CA}$ labeled nanoplatforms at indicated concentrations were added to the wells before the addition of radio-ligand (Fig. 8).

We first tested the $\gamma\text{Fe}_2\text{O}_3\text{@CA}$ nanoplatform for non-specific binding to $\alpha_v\beta_3$ and no binding was observed (Fig. 8A). The concentrations of free ligands cRGDfK and c(RGDfK)-PEG₂-NH₂ required for half-maximal competitions are 93 nM and 32 nM respectively, Table 6. Such a decrease in IC₅₀ values, comparing cRGDfK and c(RGDfK)-PEG₂-NH₂ ligands, has to be

attributed to higher hydrophilicity introducing a PEG linker on the cRGDfK ligand.

Incubation of the $\alpha_v\beta_3$ receptor with increasing concentrations of ¹²⁵I-echistatin led to a saturable binding (see ESI Fig. S12†). Non-specific binding was evaluated in the presence of 200-fold molar excess of echistatin and was negligible. Scatchard analysis of the binding gave a linear fit with a K_d of 0.22 nM. As described previously,²⁹ echistatin binds to $\alpha_v\beta_3$ in a non-dissociable manner and hence only an apparent K_d value can be assigned. Then the K_i values for various RGD nanoplatforms are deduced from the IC₅₀ values following eqn 1 (ref. 55):

$$K_i = \frac{\text{IC}_{50}}{1 + \frac{L^*}{K_d}} \quad (1)$$

As expected, K_i values for the multivalent nanoparticles are markedly decreased relative to the corresponding free ligand (Table 6). Nanoparticles bearing cRGDfK or cRGDfK-PEG₂-NH₂ ligands demonstrate equivalent affinity (K_i) for an equivalent amount of peptides per nanoparticle (Table 6): compare $R = 20$ for $\gamma\text{Fe}_2\text{O}_3\text{@CA-cRGD}$ and $R = 2$ for $\gamma\text{Fe}_2\text{O}_3\text{@CA-(PEG-cRGD)}$. Hence, the addition of PEG linker onto the nanoplatform, increasing the distance between the nanoparticle surface and the cRGD ligand, does not induce better affinity as observed with free molecules. This could be related to the short length of the PEG linker (MW 300). However, as previously described, better coverage yield is obtained with cRGDfK-PEG₂-NH₂ (see $R = 20$ Table 5) leading to a subnanomolar affinity of 0.8 nM.

Concerning the multimodal nanoplatforms, Fig. 8C shows that the two multimodal nanoplatforms present similar IC₅₀

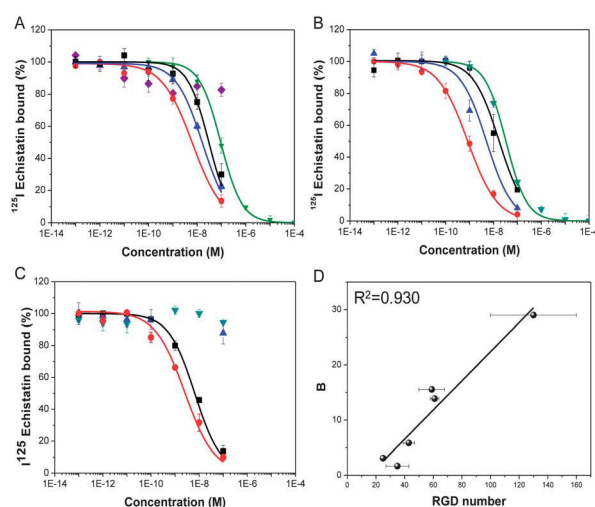


Fig. 8 ¹²⁵I-echistatin was added to a final concentration of 0.05 nM in the presence of various competing ligands at the indicated concentrations. After 3 h, the wells were washed and radioactivity was determined by gamma-counting. The ligands studied were (A) $\gamma\text{Fe}_2\text{O}_3\text{@CA}$ (purple), cRGDfK (green) $\gamma\text{Fe}_2\text{O}_3\text{@CA-cRGD}$ for a ratio $R = 0.2$ (black), $R = 2$ (blue), $R = 20$ (red); (B) cRGDfK-PEG₂-NH₂ (green), $\gamma\text{Fe}_2\text{O}_3\text{@CA-(PEG-cRGD)}$ for a ratio $R = 0.2$ (black), $R = 2$ (blue), $R = 20$ (red); (C) two step (red) and three step (black) strategies of multimodal nanoplatforms and their blanks (green) and (blue) respectively; (D) evolution of the beta factor as a function of the cRGD number.

Table 6 IC₅₀, K_i and β factor towards $\alpha_v\beta_3$, obtained by competition binding assay, of $\gamma\text{Fe}_2\text{O}_3$ @CA-cRGD and $\gamma\text{Fe}_2\text{O}_3$ @CA-(PEG-cRGD) nanoplateforms for a ratio $R = 0$, $R = 0.2$, $R = 2$ and $R = 20$

	R	Grafted molecule number		IC ₅₀ (nM)	K _i (nM)	β
		OPA	%			
cRGDfk	0	—	—	93	76	—
	0.2	25 ± 2	2 ± 0.2	30	24	3.1
	2	43 ± 4	4 ± 0.4	16	13	5.8
	20	59 ± 9	5 ± 1	6	5	16
c(RGDfk)-PEG ₂ -NH ₂	0	—	—	32	26	—
	0.2	35 ± 8	3 ± 1	17	14	1.9
	2	61 ± 3	6 ± 0.3	5	4	6.4
	20	130 ± 30	12 ± 3	0.8	0.7	40

values (3 nM and 7 nM for the two and three step strategy respectively). Moreover, the presence of the dye has no effect on IC₅₀ values (nanoplateform with cRGDfk-PEG₂-NH₂, $R = 2$ (61 cRGDfk-PEG₂-NH₂) IC₅₀ = 5 nM).

To relate K_i (multivalent) to K_i (free) where the precise number of ligand-target interactions is not known, Whitesides and colleagues defined an enhancement factor β , which increases as the relative affinity of a multivalent interaction increases: $\beta = K_i(\text{free})/K_i(\text{multivalent})$.⁵⁶ For the multivalent nanoparticles tested here, β ranges from approximately 1 to 40 and vary linearly with the number of cRGD binding sites on the surface of the nanoparticle (Fig. 8D). This is in close agreement with observations of Piletska *et al.*⁵⁷ with biotinylated nanoparticles and Soukka *et al.*⁵⁸ with antibody nanoparticles who stated that the avidity of the nanoplateform toward their respective targets is directly correlated with the number of binding sites on the nanoparticle surface.

Conclusions

A new nanoplateform has been elaborated as a dual imaging magnetic resonance/fluorescence contrast agent targeting $\alpha_v\beta_3$ integrins. For this purpose, the iron oxide NP for MR imaging has been surface functionalized with caffeic acid as a green robust anchoring agent. The free carboxylic moieties are used for the covalent coupling of various functionalities: fluorescent Rhodamine for fluorescence imaging, PEG chain as linkers and cyclic cRGD for integrin targeting. The different multimodal nanoplateforms are characterized in detail in order to control their design. We showed that the synthesized particles present T₂ MR and fluorescence contrast depending on their concentration. The specific targeting to the $\alpha_v\beta_3$ receptor has been demonstrated with a surface plasmon resonance and a solid-phase receptor-binding assay. The affinity was directly correlated with the amount of cRGD per nanoparticle and was not disturbed with dyes or PEG linker functionalities. The PEG spacer allows conjugation of a larger amount of cRGD leading to an optimized subnanomolar affinity of 0.8 nM compared to 76 nM for the free cRGD. These results added to the biostability and the PEG chains for long time blood circulation pave the way

for their *in vivo* uses in dual imaging. For the *in vivo* study the described coating process will be extended to NIR dye. In future studies, the nanoparticle size and PEG chain length should be optimized. Other specific peptides could also be conjugated to the dual MR/fluorescent probe for targeting various pathologies.

Acknowledgements

This work was supported by ANR 2010-BLAN-1007-1 funding. We are grateful to N. Lievre (University of Paris 13, Bobigny, France) for TEM observations, Magnisense Corporation for providing MIAplex Reader and to Pr. P.Y. Brillet for MRI access and Mr Steven Gressin for technical assistance (Hosp. Avicenne, Radiology department).

Notes and references

- 1 X.-H. Peng, X. Qian, H. Mao, A. Y. Wang, Z. (Georgia) Chen, S. Nie and D. M. Shin, *Int. J. Nanomed.*, 2008, **3**, 311–321.
- 2 B. Basly, D. Felder-Flesch, P. Perriat, G. Pourroy and S. Bégin-Colin, *Contrast Media Mol. Imaging*, 2011, **6**, 132–138.
- 3 S. Mornet, S. Vasseur, F. Grasset and E. Duguet, *J. Mater. Chem.*, 2004, **14**, 2161.
- 4 D. L. Thorek, A. K. Chen, J. Czupryna and A. Tsourkas, *Ann. Biomed. Eng.*, 2006, **34**, 23–38.
- 5 Q. Quan, J. Xie, H. Gao, M. Yang, F. Zhang, G. Liu, X. Lin, A. Wang, H. S. Eden and S. Lee, *Mol. Pharmaceutics*, 2011, **8**, 1669–1676.
- 6 N. T. K. Thanh and L. A. W. Green, *Nano Today*, 2010, **5**, 213–230.
- 7 S. Chen, L. Wang, S. L. Duce, S. Brown, S. Lee, A. Melzer, S. A. Cuschieri and P. André, *J. Am. Chem. Soc.*, 2010, **132**, 15022–15029.
- 8 X. Montet, M. Funovics, K. Montet-Abou, R. Weissleder and L. Josephson, *J. Med. Chem.*, 2006, **49**, 6087–6093.
- 9 F. Danhier, A. L. Breton and V. Préat, *Mol. Pharmaceutics*, 2012, **9**, 2961–2973.
- 10 D. Arosio, C. Casagrande and L. Manzoni, *Curr. Med. Chem.*, 2012, **19**, 3128–3151.
- 11 R. Max, R. R. Gerritsen, P. T. Nooijen, S. L. Goodman, A. Sutter, U. Keilholz, D. J. Ruiter and R. M. De Waal, *Int. J. cancer*, 1997, **71**, 320–324.
- 12 D. Arosio, L. Manzoni, E. M. Araldi and C. Scolastico, *Bioconjugate Chem.*, 2011, **22**, 664–672.
- 13 K. Temming, R. M. Schiffelers, G. Molema and R. J. Kok, *Drug Resist. Updates*, 2005, **8**, 381–402.
- 14 W. Cai and X. Chen, *Anti-Cancer Agents Med. Chem.*, 2006, **6**, 407–428.
- 15 G. Thumshirn, U. Hersel, S. L. Goodman and H. Kessler, *Chem.–Eur. J.*, 2003, **9**, 2717–2725.
- 16 Z. Cheng, Y. Wu, Z. Xiong, S. S. Gambhir and X. Chen, *Bioconjugate Chem.*, 2005, **16**, 1433–1441.
- 17 J. R. Baker Jr, *Chem. Commun.*, 2005, 5739–5741.
- 18 U. Hersel, C. Dahmen and H. Kessler, *Biomaterials*, 2003, **24**, 4385–4415.

- 19 E. Kluza, D. W. van der Schaft, P. A. Hautvast, W. J. Mulder, K. H. Mayo, A. W. Griffioen, G. J. Strijkers and K. Nicolay, *Nano Lett.*, 2009, **10**, 52–58.
- 20 Y.-H. Kim, J. Jeon, S. H. Hong, W.-K. Rhim, Y.-S. Lee, H. Youn, J.-K. Chung, M. C. Lee, D. S. Lee and K. W. Kang, *Small*, 2011, **7**, 2052–2060.
- 21 E. Garanger, D. Boturyn, J.-L. Coll, M.-C. Favrot and P. Dumy, *Org. Biomol. Chem.*, 2006, **4**, 1958–1965.
- 22 W. Boerjan, J. Ralph and M. Baucher, *Annu. Rev. Plant Biol.*, 2003, **54**, 519–546.
- 23 C. de Montferrand, Y. Lalatonne, D. Bonnin, N. Lièvre, M. Lecouvey, P. Monod, V. Russier and L. Motte, *Small*, 2012, **8**, 1945–1956.
- 24 Y. Lalatonne, C. Paris, J. M. Serfaty, P. Weinmann, M. Lecouvey and L. Motte, *Chem. Commun.*, 2008, 2553–2555.
- 25 F. Benyettou, Y. Lalatonne, I. Chebbi, M. Di Benedetto, J. M. Serfaty, M. Lecouvey and L. Motte, *Phys. Chem. Chem. Phys.*, 2011, **13**, 10020–10027.
- 26 F. Benyettou, E. Guenin, Y. Lalatonne and L. Motte, *Nanotechnology*, 2011, **22**, 055102.
- 27 F. Geinguenaud, I. Souissi, R. Fagard, L. Motte and Y. Lalatonne, *Nanomedicine*, 2012, **8**, 1106–1115.
- 28 R. A. Orlando and D. A. Cheresch, *J. Biol. Chem.*, 1991, **266**, 19543–19550.
- 29 C. C. Kumar, C. P. R. Huiming-Nie, M. Malkowski, E. Maxwell, J. J. Catino and L. Armstrong, *J. Pharmacol. Exp. Ther.*, 1997, **283**, 843–853.
- 30 I. A. Janković, Z. V. Saponjić, E. S. Dvzunuzović and J. M. Nedeljković, *Nanoscale Res. Lett.*, 2010, **5**, 81–88.
- 31 W. J. Barreto, R. A. Ando, B. M. Estevão and K. P. da S. Zanon, *Spectrochim. Acta, Part A*, 2012, **92**, 16–20.
- 32 M. D. Shultz, J. U. Reveles, S. N. Khanna and E. E. Carpenter, *J. Am. Chem. Soc.*, 2007, **129**, 2482–2487.
- 33 P. Z. Araujo, P. J. Morando and M. A. Blesa, *Langmuir*, 2005, **21**, 3470–3474.
- 34 S. T. Martin, J. M. Kesselman, D. S. Park, N. S. Lewis and M. R. Hoffmann, *Environ. Sci. Technol.*, 1996, **30**, 2535–2542.
- 35 C. De Montferrand, L. Hu, I. Milosevic, V. Russier, D. Bonnin, L. Motte, A. Brioude and Y. Lalatonne, *Acta Biomater.*, 2013, **9**, 6150–6157.
- 36 T. Rajh, L. X. Chen, K. Lukas, T. Liu, M. C. Thurnauer and D. M. Tiede, *J. Phys. Chem. B*, 2002, **106**, 10543–10552.
- 37 A. M. Andersen, *Acta Chem. Scand.*, 1975, **29**, 239–244.
- 38 E. Amstad, A. U. Gehring, H. Fischer, V. V. Nagaiyanallur, G. Hähner, M. Textor and E. Reimhult, *J. Phys. Chem. C*, 2011, **115**, 683–691.
- 39 E. Amstad, T. Gillich, I. Bilecka, M. Textor and E. Reimhult, *Nano Lett.*, 2009, **9**, 4042–4048.
- 40 F. Bertorelle, C. Wilhelm, J. Roger, F. Gazeau, C. Ménager and V. Cabuil, *Langmuir*, 2006, **22**, 5385–5391.
- 41 S. K. Mandal, N. Lequeux, B. Rotenberg, M. Tramier, J. Fattaccioli, J. Bibette and B. Dubertret, *Langmuir*, 2005, **21**, 4175–4179.
- 42 J. M. Perez, T. O'Loughin, F. J. Simeone, R. Weissleder and L. Josephson, *J. Am. Chem. Soc.*, 2002, **124**, 2856–2857.
- 43 A. Lorenzen and S. W. Kennedy, *Anal. Biochem.*, 1993, **214**, 346–348.
- 44 J. R. Benson and P. E. Hare, *Proc. Natl. Acad. Sci. U. S. A.*, 1975, **72**, 619–622.
- 45 S. S. Simons Jr and D. F. Johnson, *J. Org. Chem.*, 1978, **43**, 2886–2891.
- 46 S. S. Simons Jr and D. F. Johnson, *Anal. Biochem.*, 1978, **90**, 705–725.
- 47 K. Mopper and D. Delmas, *Anal. Chem.*, 1984, **56**, 2557–2560.
- 48 H. Nakamura and Z. Tamura, *Anal. Chem.*, 1981, **53**, 2190–2193.
- 49 H.-Y. Lee, Z. Li, K. Chen, A. R. Hsu, C. Xu, J. Xie, S. Sun and X. Chen, *J. Nucl. Med.*, 2008, **49**, 1371–1379.
- 50 W. Cai and X. Chen, *J. Nucl. Med.*, 2008, **49**, 113S–128S.
- 51 L. W. Dobrucki, E. D. de Muinck, J. R. Lindner and A. J. Sinusas, *J. Nucl. Med.*, 2010, **51**, 66S–79S.
- 52 X. Yang, H. Hong, J. J. Grailer, I. J. Rowland, A. Javadi, S. A. Hurley, Y. Xiao, Y. Yang, Y. Zhang and R. J. Nickles, *Biomaterials*, 2011, **32**, 4151–4160.
- 53 Y.-X. J. Wang, *Quant. Imaging Med. Surg.*, 2011, **1**, 35.
- 54 Y. Liu, Y. Pan and Y. Xu, *J. Biomol. Screening*, 2010, **15**, 131–137.
- 55 K. A. Krohn and J. M. Link, *Nucl. Med. Biol.*, 2003, **30**, 819–826.
- 56 M. Mammen, S.-K. Choi and G. M. Whitesides, *Angew. Chem., Int. Ed.*, 1998, **37**, 2754–2794.
- 57 E. V. Piletska and S. A. Piletsky, *Langmuir*, 2010, **26**, 3783–3785.
- 58 T. Soukka, H. Härmä, J. Paukkunen and T. Lövgren, *Anal. Chem.*, 2001, **73**, 2254–2260.